nature neuroscience

Spatially segregated feedforward and feedback neurons support differential odor processing in the lateral entorhinal cortex

Frauke C Leitner[1–3,6], Sarah Melzer[1,5,6], Henry Lütcke[4,5], Roberta Pinna[1,2], Peter H Seeburg[3], Fritjof Helmchen[4] & Hannah Monyer[1,2]

The lateral entorhinal cortex (LEC) computes and transfers olfactory information from the olfactory bulb to the hippocampus. Here we established LEC connectivity to upstream and downstream brain regions to understand how the LEC processes olfactory information. We report that, in layer II (LII), reelin- and calbindin-positive (RE^+ and CB^+) neurons constitute two major excitatory cell types that are electrophysiologically distinct and differentially connected. RE^+ neurons convey information to the hippocampus, while CB^+ neurons project to the olfactory cortex and the olfactory bulb. *In vivo* calcium imaging revealed that RE^+ neurons responded with higher selectivity to specific odors than CB^+ neurons and GABAergic neurons. At the population level, odor discrimination was significantly better for RE^+ than CB^+ neurons, and was lowest for GABAergic neurons. Thus, we identified in LII of the LEC anatomically and functionally distinct neuronal subpopulations that engage differentially in feedforward and feedback signaling during odor processing.

© 2016 Nature America, Inc. All rights reserved.

The LEC is involved in olfactory discrimination learning and in the integration of olfactory information into associative multimodal memories[1–4]. Olfactory information reaches the LEC directly via projections from olfactory bulb (OB) mitral cells that are the primary targets of olfactory sensory neurons[5,6]. In addition, olfactory signals are indirectly transferred to the LEC from other olfactory cortical areas including the piriform cortex (PIR)[7,8]. From the LEC, LII and LIII neurons convey olfactory information directly to the hippocampus[9]. But the LEC is more than a mere relay station for olfactory information transfer. Intricate local inhibitory–excitatory networks and feedback projections to the OB and PIR[2,10,11] suggest participation in top-down control and local processing of olfactory information. Strong interactions between olfactory areas and between LEC and hippocampus are manifested as oscillatory coupling during awake behavior[12] and associative odor–place learning[3].

Several recent studies have focused on odor information processing in excitatory and inhibitory neurons of the PIR in rodents[13,14]. This is in stark contrast to the scarcity of information on odor processing in defined neurons in the LEC. Odor-responsive neurons are found in both superficial and deep layers of the LEC[3,15,16]. LII is of particular interest since its principal cell types are the recipients of direct OB input and the direct source of feedforward and feedback projections[2,17]. *In vitro* studies suggest that LII of LEC comprises several excitatory and inhibitory cell types[18–20], but it is not known how these neuronal cell types contribute to odor processing. To address this question, we used *in vivo* two-photon calcium imaging of odor-evoked responses in LEC neurons in anesthetized mice. We combined calcium imaging of identified GCaMP6-expressing neurons with targeted whole-cell patch-clamp recordings, anatomical tracing techniques and immunolabeling of marker proteins for a functional characterization of distinct cell types *in vitro* and *in vivo*.

RESULTS

Spatial segregation and differential projection of RE^+ and CB^+ neurons

Two sublayers can be distinguished in LII of the LEC[21], which we refer to henceforth as LIIa and LIIb. We first performed immunohistochemistry to establish the identity of excitatory neurons in $Gad1^{EGFP}$ (in the following referred to as $GAD67^{EGFP}$) mice to exclude inhibitory neurons. The choice of marker proteins was prompted by results reported for the adjacent medial entorhinal cortex (MEC), where RE and CB immunolabeling delineates two almost non-overlapping excitatory cell populations in LII[22–25]. Indeed, in LII of the LEC as well, the two markers were expressed in distinct cell populations that segregated with respect to their localization. RE^+ neurons formed a narrow band of densely packed neurons in LIIa, whereas CB^+ neurons tended to cluster in LIIb. RE^+ neurons represent $97.7 \pm 0.1\%$ of all excitatory neurons in LIIa, while excitatory CB^+ neurons represent $69.3 \pm 5.1\%$ of all excitatory neurons in LIIb (**Supplementary Fig. 1**). Much like the expression pattern in the MEC[23], albeit to a slightly lesser degree,

[1]Department of Clinical Neurobiology at the Medical Faculty of Heidelberg University, Heidelberg, Germany. [2]German Cancer Research Center (DKFZ), Heidelberg, Germany. [3]Department of Molecular Neurobiology, Max Planck Institute for Medical Research, Heidelberg, Germany. [4]Laboratory of Neural Circuit Dynamics, Brain Research Institute, University of Zurich, Zurich, Switzerland. [5]Present addresses: Department of Neurobiology, Howard Hughes Medical Institute, Harvard Medical School, Boston, Massachusetts, USA (S.M.). and Scientific IT Services, ETH Zurich, Zurich, Switzerland (H.L.). [6]These authors contributed equally to this work. Correspondence should be addressed to H.M. (h.monyer@dkfz-heidelberg.de).

Received 31 July 2015; accepted 20 April 2016; published online 16 May 2016; doi:10.1038/nn.4303

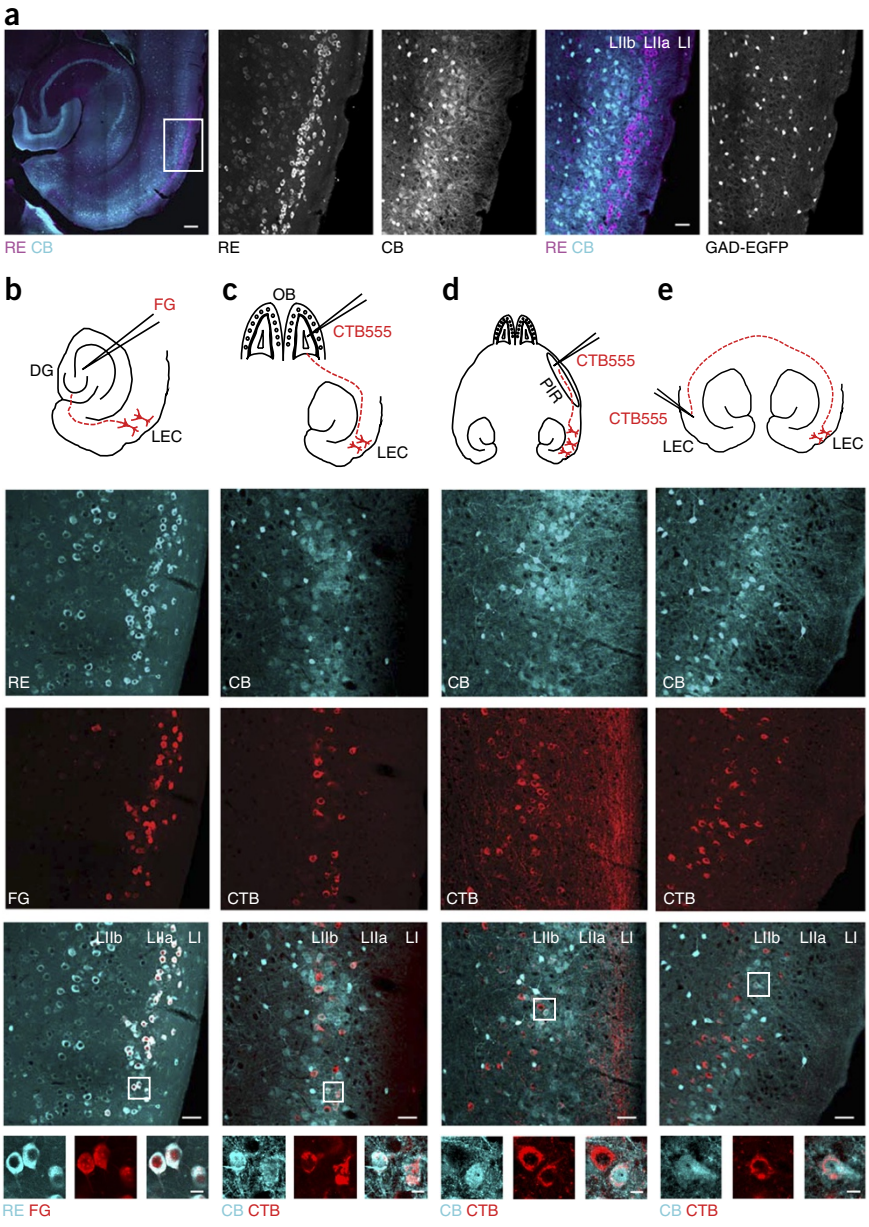

Figure 1 Differential projection patterns of LEC LII excitatory neurons: RE$^+$ neurons provide feedforward projections to the hippocampus while CB$^+$ neurons project to OB, PIR and contralateral LEC. (**a**) Left panel: confocal image of the hippocampus and parahippocampal region in a *GAD67^{EGFP}* mouse immunostained against RE and CB. The right four images show a higher magnification of the boxed area and the corresponding image of endogenous EGFP fluorescence. Scale bars, 200 µm (left) and 50 µm. (**b**) FG injection site in the dentate gyrus (DG) and the area of analysis in the LEC. The two panels below depict RE-immunostained and FG$^+$ neurons, followed by a merged image. Small panels underneath show higher magnifications of the boxed area. (**c**) CTB injection site in the OB, and the area of analysis in the LEC. The two panels underneath show higher magnifications of the boxed area. (**d**) Same as in **c**, except that CTB was injected in the PIR. (**e**) Same as in **c**, but with tracer injection in the contralateral LEC. Confocal images of injection sites and images of the LEC in horizontal brain slices immunostained against CB or RE following injections of FG into the dentate gyrus, and injections of CTB into OB, PIR or contralateral LEC, respectively, are shown in **Supplementary Figure 1**. Scale bars in **b** to **e**, 50 µm (main panels) and 10 µm (bottom row).

CB expression in the LEC revealed a modular organization. EGFP$^+$ GABAergic neurons were distributed across all layers (**Fig. 1a**).

To determine the projection pattern of RE$^+$ and CB$^+$ neurons, we injected retrograde tracers in putative target areas (Online Methods). Fluorogold (FG) injection into the dentate gyrus yielded a dense band of retrogradely labeled FG$^+$ neurons in LIIa. Almost all FG$^+$ neurons were RE$^+$ (98.3 ± 0.6%, mean ± s.e.m.), and a small fraction (0.6%) were GABAergic neurons (**Fig. 1b**; 1,097 FG$^+$ neurons counted, 2 hemispheres, 2 *GAD67^{EGFP}* mice). In contrast, injection into OB of the retrograde tracer cholera toxin subunit B (CTB) resulted in dense labeling of LIIb neurons. Of the retrogradely labeled neurons, 69.2 ± 0.6% were CB$^+$ (**Fig. 1c**; 1,107 CTB$^+$ neurons counted, 4 hemispheres, 1 wild-type mouse and 2 *GAD67^{EGFP}* mice). A minority of CTB$^+$ cells were located in LIIa, of which a third were RE$^+$ (191 CTB$^+$ neurons counted, 4 hemispheres, 1 wild-type mouse and 2 *GAD67^{EGFP}* mice). There were no CTB$^+$ GAD67-EGFP$^+$ neurons. Following injections of CTB into PIR, retrogradely labeled neurons were detected preferentially in LIII and deeper layers (**Fig. 1d**). We identified CTB$^+$ neurons also in LIIb, of which 53.2 ± 5.9% stained for CB (239 CTB$^+$ neurons counted, 3 hemispheres, 3 wild-type mice). CTB$^+$ neurons were rarely detected in LIIa. Finally, we investigated whether CB$^+$ neurons participate in the interhemispheric connectivity between the two LECs. Injection of CTB into one LEC resulted in retrogradely labeled neurons in the contralateral LEC. Thus, about half of the CTB$^+$ neurons in LIIb were CB$^+$ (**Fig. 1e**; 183 out of 335 CTB$^+$ neurons counted, 2 wild-type mice).

Expression analysis of RE and CB in LII of the LEC indicated that there was almost no co-expression of the two markers. This corresponds with the differential projection pattern of the two cell populations (see also **Supplementary Fig. 2**).

Heterogeneous GABAergic neurons in LII

To investigate the molecular identity of GABAergic neurons, we employed *GAD67^{EGFP}* mice. Parvalbumin-positive (PV$^+$) neurons represented 17.4 ± 1.7% and 30.3 ± 4.3% (mean ± s.e.m.) of GABAergic neurons in LIIa and LIIb, respectively. Somatostatin-positive (SOM$^+$) and calretinin-positive (CR$^+$) neurons represented smaller GABAergic populations (6.8 ± 2.7% and 14.3 ± 1.8% SOM$^+$ neurons, and 18.1 ± 2.4% and 27.0 ± 1.8% CR$^+$ neurons in LIIa and LIIb, respectively). Together these data suggest that another GABAergic subpopulation must be prevalent in the superficial layers of LEC. Indeed, type 3A serotonin receptor–expressing (5-HT$_{3A}$R$^+$) GABAergic neurons (which include some CR$^+$ subtypes[26]) accounted for 60.3 ± 4.6% and 51.0 ± 1.2% of all GABAergic neurons in LIIa and LIIb, respectively. RE and CB were detected also in a fraction of GABAergic neurons. Thus, 51.0 ± 4.4% of GABAergic neurons in LIIa were

© 2016 Nature America, Inc. All rights reserved.

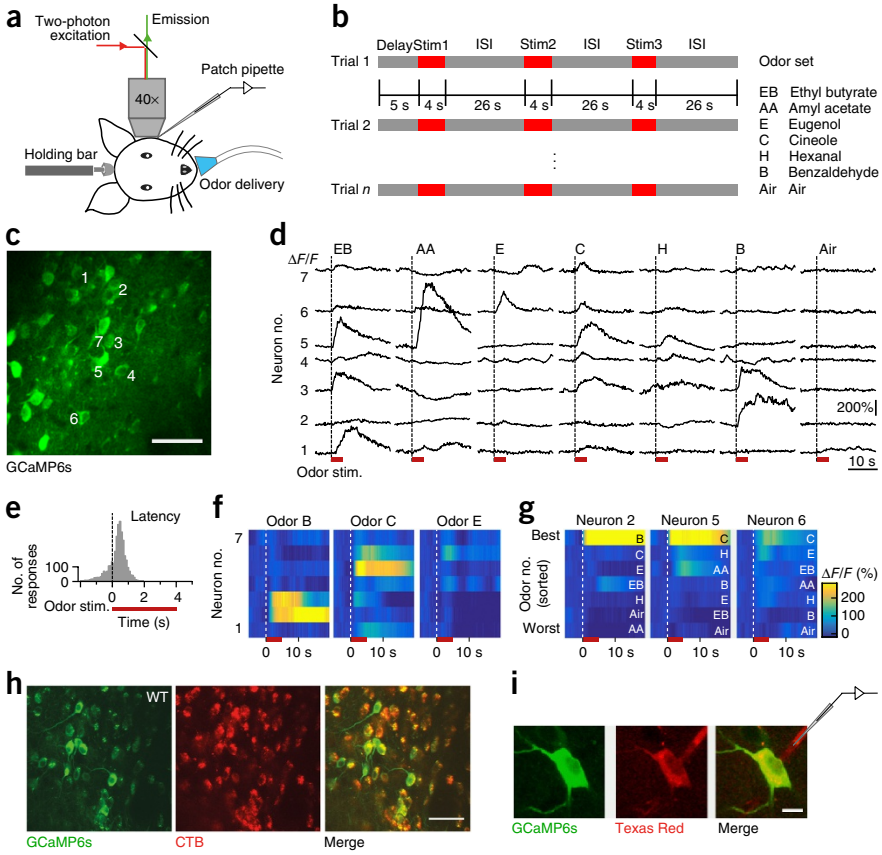

Figure 2 Odor-evoked calcium transients in LEC LII neurons are variable. (**a**) Experimental setup for *in vivo* imaging of LEC neurons. (**b**) Odor stimulation protocol and list of applied odors. Stim, stimulus; ISI, interstimulus interval. (**c**) *In vivo* two-photon image showing GCaMP6-expressing LEC LII neurons. Scale bar, 50 µm; numbers mark example neurons. (**d**) Odor-evoked calcium transients in the seven neurons marked in the population shown in **c**. Shown are single-trial responses to the indicated odors. (**e**) Histogram of onset latency from stimulation start, estimated by linearly fitting calcium transient onsets for responsive neurons. (**f**) Color map representation of the average calcium responses for three odors across the example population of seven neurons shown in **d** (averages of 6, 9 and 6 trials for odors B, C and E, respectively). (**g**) Color map representation of average odor response patterns ('receptive fields') for three example neurons. Receptive fields were sorted from best to worst odor for each neuron as indicated. (**h**,**i**) *In vivo* calcium imaging and targeted electrophysiology of identified LII neurons. In this example, calcium imaging was performed in dentate-gyrus-projecting neurons identified by retrograde tracer injection into the hippocampus. Neurons were tested for odor responsiveness, and *in vivo* or *in vitro* electrophysiological studies combined with cell reconstruction of biocytin-filled neurons were carried out subsequently. Scale bars, 50 µm in **h** and 10 µm in **i**.

© 2016 Nature America, Inc. All rights reserved.

RE$^+$, and 37.9 ± 3.4% in LIIb were CB$^+$ (for quantitative evaluation see **Supplementary Fig. 3**).

Odor-responsive neurons in LII of the LEC

We next employed *in vivo* calcium imaging to functionally characterize LEC LII neurons. We virally induced expression of GCaMP6 in LEC neurons and performed two-photon calcium imaging of neuronal responses to odor stimulation in anesthetized mice (**Fig. 2a–c**; Online Methods). We selected six odors: ethyl butyrate, amyl acetate, eugenol, cineole, hexanal and benzaldehyde. Stimulation with air was used as control. Odors and control were presented for 4 s, with 26-s interstimulus intervals, in a randomized order to avoid sensory adaptation. Each trial consisted of three odor stimulations. For every imaging area, we recorded the neuronal responses to 5–9 stimulations per odor. Given the long duration of the stimulus protocol and the challenging surgical access to the LEC, the number of applied odors was restricted, and in most experiments we tested a single concentration for each odor (for some experiments a range of concentrations was used; see Online Methods and **Supplementary Fig. 4**).

In individual imaging areas, containing 3 to 50 neurons (median 26), a large fraction of LII neurons responded for at least one odor with a significant GCaMP6 fluorescence change during the 4-s stimulation period (79%; 1,537 of 1,950 cells total; **Fig. 2d** and Online Methods). Most of these neurons (77%) exhibited an increase in fluorescence (F) at least once (amplitude range 4% to 865% $\Delta F/F$). A substantial fraction (37%) also showed a decrease in fluorescence for at least one odor (amplitude range −6% to −37% $\Delta F/F$). Onset latencies were estimated from the initial GCaMP6 fluorescence change and displayed a narrow distribution, peaking 0.4 s after odor stimulation onset (half-width 0.6 s; **Fig. 2e**). Calcium transients lasted for several seconds (full width at half-maximum 9.53 ± 0.05 s; mean ± s.e.m.; n = 4,014 responses) and about half of all neurons (47%) displayed an additional late fluorescence increase following stimulus offset (46.6 ± 1.3% extra $\Delta F/F$ amplitude; n = 1,415 responses). Neurons differed in their response to the presentation of specific odors, thus giving rise to distinct activity patterns across the neuronal population (**Fig. 2f**). Responsive neurons differed in their odor preference (which odor elicited the largest response) and in their degree of selectivity (the broadness of calcium transient amplitude distribution across the six odors, ranked from highest to lowest). Some neurons responded to only one or a few odors, whereas others were more broadly tuned and responded to the entire panel of presented odors (**Fig. 2g**).

We wondered whether this heterogeneity in odor responses and tuning preference of LII neurons might result at least in part from differential odor processing in specific subpopulations. Thus, we first characterized LII neurons at the electrophysiological and morphological level (exemplified for dentate-gyrus-projecting neurons in **Fig. 2h**,**i**) and subsequently analyzed odor-evoked calcium transients in defined cell types.

Morphological and electrophysiological features of odor-responsive LIIa RE$^+$ neurons

To visualize odor-evoked activity specifically in RE$^+$ neurons, we injected the adeno-associated viral (AAV) vector AAV1.Syn.GCaMP6s into the LEC of wild-type mice, in which RE$^+$ cells were retrogradely labeled by CTB injection into the dentate gyrus. Odor stimulation induced clearly detectable calcium transients in CTB$^+$ neurons (**Fig. 3a**). To study morphological and electrophysiological properties of hippocampus-projecting odor-responsive neurons, we performed two-photon targeted *in vivo* whole-cell recordings with

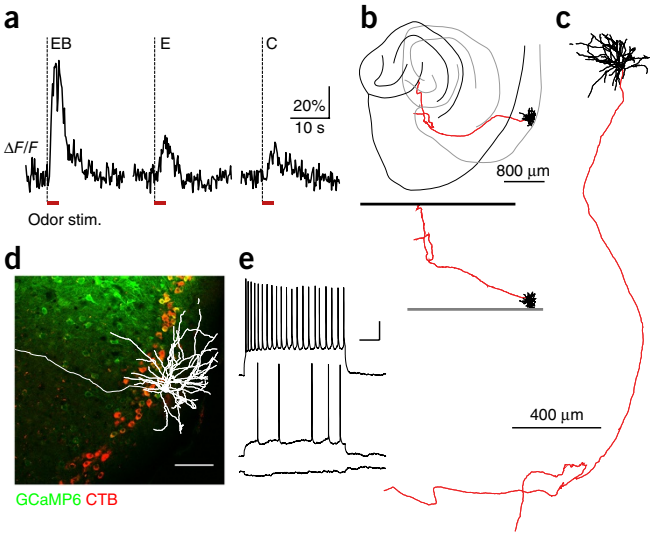

Figure 3 Odor-responsive regular spiking neurons project to the hippocampus. (**a**) Calcium transients of a RE$^+$ neuron in LIIa upon odor stimulation with ethyl butyrate (EB), eugenol (E) and cineole (C). (**b**) Reconstruction of the same neuron (cell body and dendrites in black) with good recovery of the axon (red) that projects to the hippocampus. 2D image shows a ventral (gray) and dorsal (black) outline of the hippocampus and LEC. Cell body and dendrites are localized more ventrally, whereas the axon extends to dorsal areas. The reconstructed neuron is shown along the dorsal-ventral axis (top) and along the posterior-anterior axis (bottom). (**c**) Higher magnification of the same reconstructed neuron. (**d**) *Ex vivo* confocal image overlaid with the reconstructed neuron (white) confirms the cell localization in upper LIIa of the LEC. Scale bar, 100 µm. (**e**) Firing pattern of the same neuron patch-clamped *in vivo* and filled with biocytin upon –50 pA current injection, at action potential threshold and at maximal firing frequency (from bottom to top). Scale bar, 20 mV, 200 ms.

biocytin-filled patch-clamp pipettes. In five filled and reconstructed odor-responsive neurons, we detected an axon directed toward the angular bundle (n = 5 neurons in 5 mice). Three of these axons could be followed all the way to the superficial layers of para- and presubiculum, where they bent rostro-dorsally to run along the dentate gyrus border (**Fig. 3b**,**c** and **Supplementary Fig. 5**). The axon of one odor-responsive cell could be traced into the hippocampus (**Fig. 3b**,**c**). Odor-responsive neurons showed fan-like or multipolar dendritic trees that were restricted to the superficial layers and displayed either a regular adapting or bursty action potential firing pattern upon current injection (**Fig. 3d**,**e** and **Supplementary Fig. 5**). Similar electrophysiological and morphological properties were found in additional principal neurons in LIIa that were recorded but not odor-stimulated (n = 11 neurons in 8 mice; **Supplementary Fig. 6**; for a listing of electrophysiological properties of all RE$^+$ neurons see **Supplementary Table 1**).

Morphological and electrophysiological features of LIIb CB$^+$ neurons

To examine whether CB$^+$ neurons in LIIb respond to odors, we expressed GCaMP6 cell type specifically, using *Calb1*^{Cre} (hereafter referred to as *CB*^{Cre}) mice[25]. Indeed, CB$^+$ neurons exhibited calcium transients elicited by odor presentation (**Fig. 4a**). Since the deeper localization of CB$^+$ neurons hampered *in vivo* two-photon

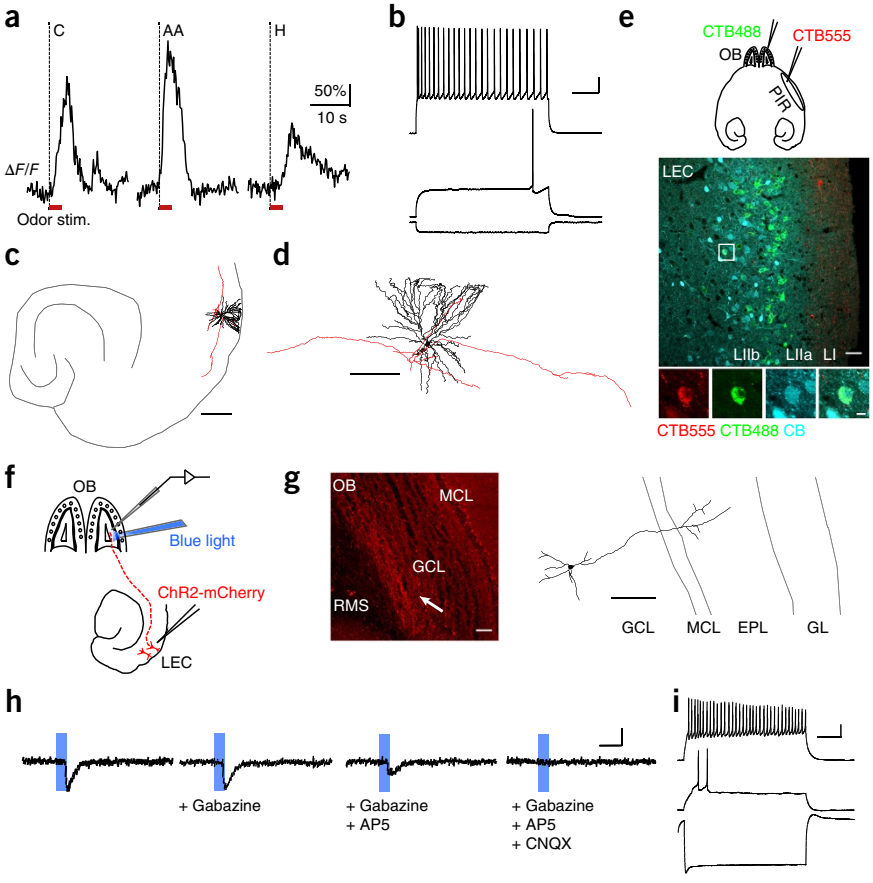

Figure 4 CB$^+$ neurons in the LEC provide feedback to the OB and the PIR. (**a**) Calcium transients of CB$^+$ neuron in LIIb upon odor stimulation with amyl acetate (AA), cineole (C) and hexanal (H). (**b**) Typical firing pattern of a CB$^+$ neuron patch-clamped *in vitro* at –200 pA current injection, action potential threshold and maximal firing frequency (from bottom to top). Scale bar, 20 mV, 200 ms. (**c**) Reconstruction of the same neuron with dendrites shown in black and axon in red. Scale bar, 400 µm. (**d**) Higher magnification of the reconstructed neuron shown in **c**. Scale bar, 200 µm. (**e**) Visualization of double-labeled CB$^+$ neurons in LIIb, following injection of the retrograde tracers CTB488 in the OB and CTB555 in the PIR. Panels below show higher magnifications of the boxed area. Scale bars, 50 µm (top) and 10 µm (bottom). Line drawing (above) depicts injection sites. (**f**) AAV DIO *ChR2-mCherry* injection site and target cells recording site. (**g**) Left, confocal maximum intensity projection image of mCherry-labeled axons in the OB; arrow, highest density of fibers in deep granule cell layer (GCL). Right, reconstruction of a granule cell that responded to optogenetic stimulation. Scale bars, 100 µm. MCL, mitral cell layer; RMS, rostral migratory stream; EPL, external plexiform layer; GL, glomerular layer. (**h**) Postsynaptic currents in a target cell at –70 mV holding potential with indicated antagonists. Scale bars, 10 ms and 10 pA. (**i**) Representative firing pattern of a target cell in the OB showing traces at –200 pA current injection, action potential threshold and maximal firing frequency (from bottom to top). Scale bars, 200 ms and 20 mV.

© 2016 Nature America, Inc. All rights reserved.

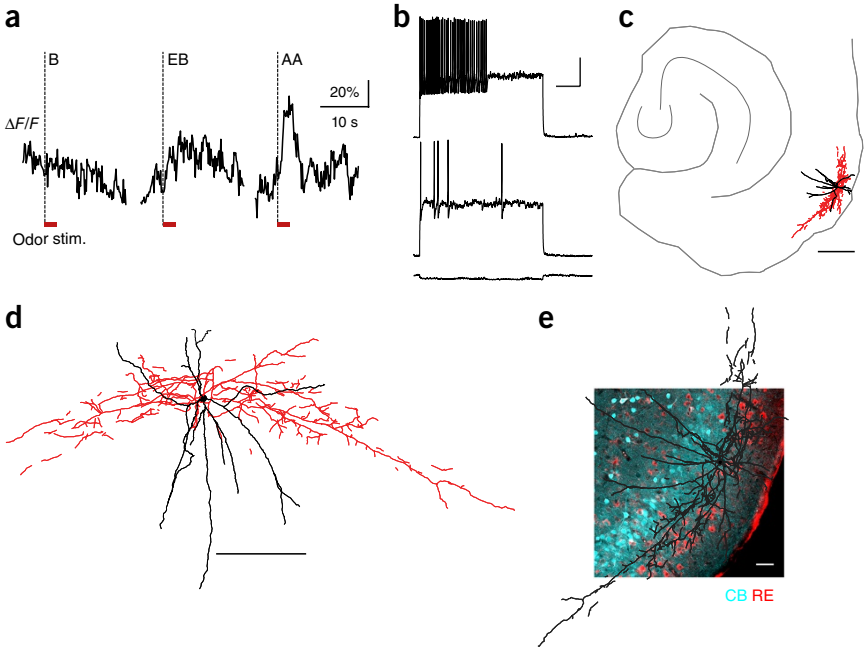

Figure 5 Fast-spiking GABAergic basket cells in the LEC are odor-responsive. (**a**) Calcium transient of GABAergic neuron in LIIa upon odor stimulation with amyl acetate (AA), benzaldehyde (B) and ethyl butyrate (EB). (**b**) Firing pattern of the same neuron patch-clamped *in vivo* and filled with biocytin upon −50 pA current injection, at action potential threshold and maximal firing frequency (from bottom to top). Scale bar, 20 mV, 200 ms. (**c**) Reconstructed neuron exhibits dendrites in superficial and deeper layers (cell body and dendrites in black) and axonal arborization in LII (red). Scale bar, 400 µm. (**d**) Higher magnification of the reconstructed neuron. Scale bar, 200 µm. (**e**) *Ex vivo* confocal image of the reconstructed neuron after immunostaining with RE and CB confirms the cell localization in LIIa of the LEC. Scale bar, 50 µm.

targeted patch-clamp recordings, we analyzed their electrophysiological and morphological properties using targeted recordings *in vitro*. Most GCaMP6-labeled cells in LIIb of injected CB^{Cre} mice were principal neurons as indicated by their regular adapting spiking behavior and the presence of spiny dendrites (32 out of 43 neurons in 9 mice, **Fig. 4b**). CB^+ principal neurons exhibited multiform (14 out of 32 neurons), oblique pyramidal (11 out of 32 neurons) or pyramidal (7 out of 32 neurons) morphology (**Supplementary Fig. 7c**). Axons exhibited a preferred horizontal extension within superficial layers of the LEC (9 out of 10 reconstructed neurons, **Fig. 4c**,**d** and **Supplementary Fig. 7c**). The recorded CB^+ neurons also included a mixed population of putative GABAergic neurons (11 out of 43 neurons in 9 mice).

A direct comparison of CB^+ and RE^+ neurons studied *in vitro* highlights differences of the intrinsic properties (**Supplementary Fig. 7a**). *K*-means cluster analysis based on electrophysiological parameters (Online Methods) revealed two cell clusters that largely corresponded (64 out of 70 neurons) to RE^+ and CB^+ neurons (**Supplementary Fig. 7d**). RE^+ neurons exhibited multiform (11 out of 22 neurons) or fan-like (11 out of 22 neurons) morphology (**Supplementary Fig. 7b**). Consistent with previous literature, neither RE^+ nor CB^+ cell morphology could be predicted on the basis of their electrophysiological properties[19].

Since CB^+ LIIb neurons project to the OB and the PIR, we wondered whether individual CB^+ neurons target both areas. We thus injected the retrograde tracers CTB488 (green) and CTB555 (red) into the OB and the PIR, respectively, and investigated the presence of double-labeled neurons in LIIb in the LEC. Indeed, 67 of 562 $CTB488^+$ (OB-projecting) and of 322 $CTB555^+$ (PIR-projecting) neurons were double positive for the two tracers, and a subset of these neurons expressed CB (3 mice, **Fig. 4e**).

The presence of projections from CB^+ LIIb neurons to olfactory areas upstream of the LEC in the olfactory pathway raised the question as to the identity of the targeted neurons. We hence injected double-*loxP*-flanked inverted *ChR2-mCherry* into the LEC of CB^{Cre} mice and performed *in vitro* patch-clamp experiments in OB slices (**Fig. 4f**). Notably, the $mCherry^+$ axonal fibers were preponderantly localized in close proximity to the rostral migratory stream (**Fig. 4g**). Upon light stimulation of axonal terminals, we detected responses in adjacent OB granule cells (19 responding neurons of 127 patched cells in 11 mice). The evoked responses were glutamatergic, as they were blocked with specific antagonists for NMDA receptors (D-AP5, 50 µM) and AMPA receptors (CNQX, 10 µM), but not GABAergic receptors (gabazine, 10 µM) (**Fig. 4h**,**i**, $n = 4$ cells in 3 mice).

Morphological and electrophysiological features of odor-responsive LII GABAergic neurons

To investigate odor responsiveness of GABAergic neurons in LII of the LEC, we injected AAV1.Syn.flex.GCaMP6s into $GAD67^{Cre}$ mice. Clear odor-evoked calcium transients occurred in LII GABAergic neurons (**Fig. 5a**). On the basis of the *in vivo* firing pattern and morphology, we identified all successfully recorded and reconstructed odor-responsive cells as typical GABAergic neurons (4 out of 4 neurons in 4 mice, **Fig. 5b**–**e** and **Supplementary Fig. 8**). The maximal firing rate of GABAergic neurons was higher than the maximal firing rate of *in vivo* patched principal cells in LIIa (48.5 ± 7.2 Hz versus 22.5 ± 1.5 Hz in RE^+ neurons, mean ± s.e.m., $t_{(3.26)} = -3.54$, $P = 0.03$). The axons were largely confined to superficial layers of the LEC and had high local densities never observed for principal cells. An additional set of GABAergic neurons patched without odor-stimulation ($n = 5$ neurons in 5 mice) had a similarly dense axonal plexus in superficial layers, suggesting that this is a common feature of GABAergic neurons in LII of the LEC (**Supplementary Fig. 9**).

Odor-responsive GABAergic neurons exhibited a range of electrophysiological and morphological properties. They comprised fast-spiking and non-fast-spiking neurons (maximal firing rate: 38–69 Hz) with accommodating or non-accommodating firing properties. They had a highly divergent input resistance (36–167 MΩ) and variable excitability (rheobase: 0–550 pA), suggesting that odor representations involve the recruitment of different types of GABAergic neurons (**Supplementary Fig. 3**; for a listing of electrophysiological properties of all GABAergic neurons, see **Supplementary Table 1**).

Cell-type-specific odor processing in LEC LII neurons

To investigate whether the three cell types process odor information in a similar fashion, we compared odor-evoked calcium transients in identified RE^+, CB^+ and GABAergic neurons (**Fig. 6a**,**b**). The 1,950 imaged neurons could be subdivided as follows: 514 RE^+ neurons (19 imaging areas in 7 mice), 407 CB^+ neurons (17 imaging areas in 8 mice), 194 GABAergic neurons (26 imaging areas in 11 mice), and

© 2016 Nature America, Inc. All rights reserved.

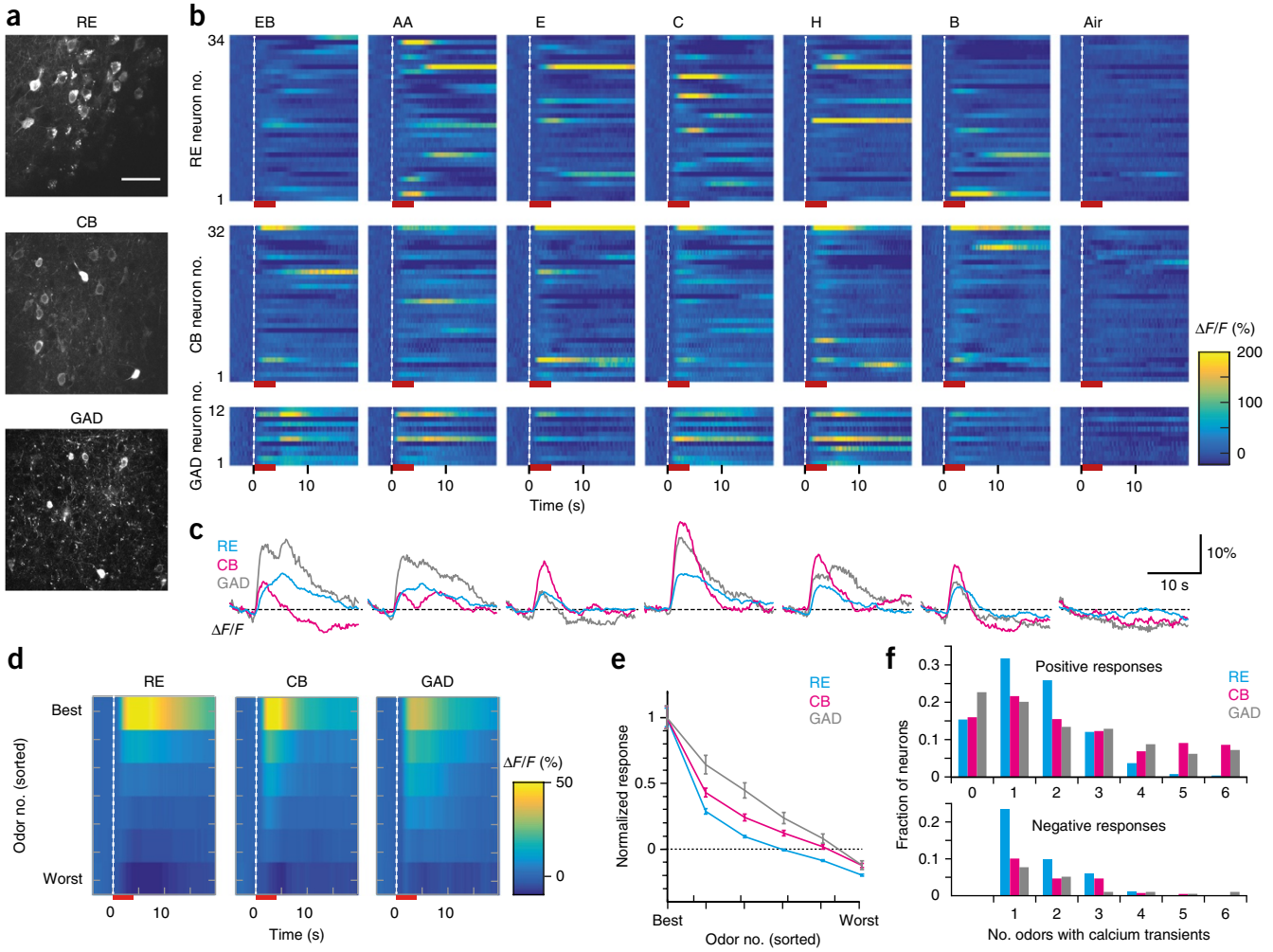

Figure 6 Odor stimulation evokes cell-type specific activity patterns in defined populations of LEC neurons. (**a**) Example two-photon images of RE$^+$ (top), CB$^+$ (middle) and GABAergic (GAD$^+$, bottom) neurons. Scale bar, 50 µm. (**b**) Average calcium responses evoked by six odors plus air in the populations in **a**. Trials per odor for RE$^+$ neurons: 9, 5, 7, 6, 7, 8, 6; CB$^+$ neurons: 7, 7, 6, 6, 6, 6, 7; GABAergic neurons: 6, 7, 7, 5, 9, 8, 6. AA, amyl acetate; B, benzaldehyde; C, cineole; EB, ethyl butyrate; E, eugenol; H, hexanal. (**c**) Average calcium responses for all odors across the entire RE$^+$, CB$^+$ and GABAergic populations (514, 407 and 194 neurons, respectively). (**d**) Odor-evoked receptive fields averaged over all RE$^+$, CB$^+$ and GABAergic neurons. Receptive fields are sorted according to best odor response for each neuron, ranked according to the mean $\Delta F/F$ amplitude of trial-averaged traces 2–3 s after stimulus onset. (**e**) Mean calcium response amplitudes as defined in **d** as a function of ranked odors, normalized to the best-odor response. Note that negative values can arise due to decreasing fluorescence responses (see also **Supplementary Fig. 10**). The difference between RE$^+$ neurons and the other cell types reaches a significance level of $P < 0.001$ for the second to fifth odor and $P < 0.01$ for the sixth odor; for CB$^+$ neurons versus GABAergic neurons $P < 0.01$ for the second and third odor, $P < 0.05$ for the fourth odor; all others are non-significant (unpaired t-tests). Error bars indicate 1 s.e.m. (**f**) Fraction of neurons for each cell type that significantly respond (either positively or negatively) to the indicated number of odors.

835 unclassified neurons (35 imaging areas in 14 mice; not considered for further analysis). Across all odors, the three subpopulations displayed complex and distinct temporal profiles of their mean calcium transients, which differed for instance in early fluorescence increase or decrease during stimulation and in the apparent late offset response component (**Fig. 6c**).

In all cell types, a substantial fraction of neurons exhibited significant mean calcium responses upon stimulation for at least one odor (85% RE$^+$, 84% CB$^+$ and 77% GABAergic neurons). For neurons exhibiting a significant fluorescence increase during the stimulation period, the mean $\Delta F/F$ peak amplitude evoked by each neuron's best odor was comparable for RE$^+$ and CB$^+$ neurons (80.8 ± 5.8% and 88.4 ± 6.6%, respectively; $n = 383$ and 301 cells; $t_{(682)} = -0.87$, $P = 1.0$), and lower for GABAergic neurons (61.7 ± 5.3%; $n = 133$; $t_{(432)} = -2.5432$, $P = 0.034$ for CB$^+$ versus GABAergic neurons; $t_{(514)} = -1.8652$, $P = 0.188$ for RE$^+$ versus GABAergic neurons; unpaired t-test, Bonferroni-corrected). These values may not be directly comparable, however, because evoked calcium transients depend on various cell type-specific factors, such as spike pattern, spike-associated calcium influx and calcium handling. Across all odors, RE$^+$ neurons showed on average positive responses to fewer odors compared to CB$^+$ and GABAergic neurons (1.89 compared to 2.89 and 2.84 odors, respectively). Notably, a high fraction of responsive RE$^+$ neurons (48%) displayed a negative early response for at least one odor. The fraction of neurons exhibiting a negative early response was lower for CB$^+$ (25%) and GABAergic (21%) neurons. Estimated onset latencies of calcium transients were not measurably different among cell types ($P = 1.0$ for all three comparisons, unpaired t-test, Bonferroni-corrected),

© 2016 Nature America, Inc. All rights reserved.

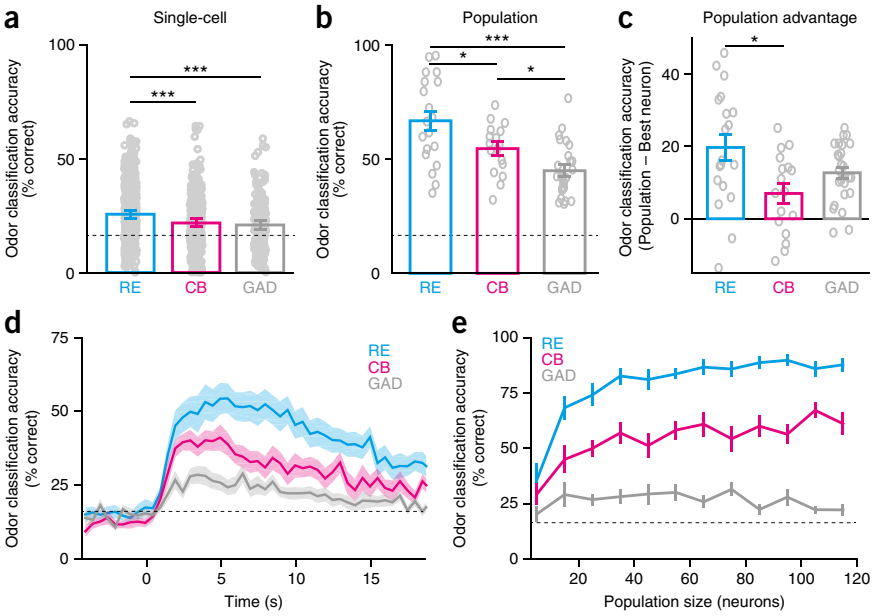

Figure 7 Populations of LEC RE$^+$ neurons encode specific odors with high accuracy. (**a**) Prediction of presented odors from calcium responses of individual neurons using a Bayesian classifier (see Online Methods). Average classification accuracy is better than chance level (16.7% for the six odors; dashed line) for all three cell types. (**b**) Prediction of presented odors from population calcium responses (averaged across imaging areas). Populations of RE$^+$ neurons allow significantly better odor classification than populations of CB$^+$ and GABAergic neurons. (**c**) Population activity of RE$^+$ neurons yields improved odor classification compared to that of the single best performing neurons in the respective cell population (imaging area). Odor discrimination of CB$^+$ and GAD$^+$ populations, by contrast, is determined more by discrimination accuracy of the best performing neuron. (**d**) Time course of population odor classification performance relative to stimulus onset. Populations of all three cell types show prolonged increase in odor prediction following odor onset. Classification accuracy is best in RE$^+$ populations, followed by CB$^+$ and GABAergic populations. (**e**) Odor classification accuracy improves for RE$^+$ and CB$^+$ populations as more neurons are included in the population. Larger GAD$^+$ populations, by contrast, do not allow better odor prediction. Note that different population sizes here were obtained by randomly sampling neurons from the entire pool of recorded neurons (i.e., from different imaging areas and mice). ***$P < 0.001$; **$P < 0.01$; *$P < 0.05$, unpaired t-test. Error bars and shaded regions indicate 1 s.e.m.

which may be due to our limited time resolution. Cell types differed, however, in their response duration, with CB$^+$ neurons generating significantly shorter mean calcium transients (full-width at half-maximum for RE$^+$ 10.24 ± 0.17 s; CB$^+$ 8.46 ± 0.17 s; GABAergic neurons 9.72 ± 0.24 s; mean ± s.e.m.; $P < 0.001$ for CB$^+$ versus others; Wilcoxon rank-sum test; n = 1,063, 1,029, and 444 responses, respectively; for example traces and distributions across cell types see **Supplementary Fig. 10**).

The finding that RE$^+$ neurons responded on average to fewer odors than the other two cell types indicates differences in odor selectivity. We further compared odor-tuning properties across cell types by averaging the ranked responses of each neuron from best to worst (**Fig. 6d**). RE$^+$ neurons displayed high response selectivity (large differences between best and second-best odor response) whereas CB$^+$ and GABAergic neurons were less selective (i.e., more broadly tuned). To quantify odor selectivity, we normalized evoked calcium responses and ranked them to the mean best odor evoked amplitude for each cell type. The resulting tuning curve declined more steeply for RE$^+$ neurons than for CB$^+$ neurons and GABAergic neurons (**Fig. 6e**; for P-values see figure legend). As another measure of tuning sharpness, we also analyzed the lifetime sparseness of the amplitude distributions, which was highest for RE$^+$ neurons, confirming their higher odor selectivity (**Supplementary Fig. 11**). As a third measure, we analyzed how many odors evoked significant positive (or negative) GCaMP6 fluorescence transients in each neuron of the three cell types. RE$^+$ neurons comprised a large fraction of neurons that responded to 1–3 odors (69.7%; compared to 49.4% and 46.4% for CB$^+$ and GABAergic neurons, respectively), while a large fraction of CB$^+$ and GABAergic neurons responded to 4–6 odors (**Fig. 6f**). Notably, RE$^+$ neurons also showed the highest fraction of selective negative responses, often to one of the six odors (**Fig. 6f**). We conclude that cell types differ in their odor tuning properties, with RE$^+$ cells featuring the highest response selectivity.

Finally, we analyzed the ability of single neurons and of the three neuronal subpopulations to decode the presented odors using a Bayesian classifier with cross-validation (Online Methods). Individual neurons decoded the six odors mostly above chance level, varying in their performance between 0 and 67% correct (chance level 16.7%). On average, individual RE$^+$ neurons performed significantly better than CB$^+$ and GABAergic neurons (25.61 ± 0.56%, 21.8 ± 0.59% and 20.9 ± 0.81% for RE$^+$, CB$^+$ and GABAergic neurons, respectively; mean ± s.e.m.; n = 514, 407 and 194; $t > 3.6$, $P < 0.01$ for RE$^+$ versus CB$^+$ and GABAergic neurons, unpaired t-tests with Holm-Bonferroni correction; **Fig. 7a**). Similar results were obtained using an information metric to quantify the mutual information between neuronal responses and odor stimulation (**Supplementary Figs. 12** and **13**). These results indicate that odor-evoked responses of individual RE$^+$ neurons contain more stimulus-specific information than those of CB$^+$ and GABAergic neurons, in line with the higher selectivity of RE$^+$ cells.

At the population level, odor classification was significantly better for RE$^+$ populations compared to CB$^+$ and GABAergic populations (n = 19, 17 and 26 RE$^+$, CB$^+$ and GABAergic neuron populations; $t > 2.3$, $P < 0.03$ for all three comparisons, unpaired t-tests with Holm-Bonferroni correction; **Fig. 7b**). This finding is consistent with the heterogeneous but more selective odor response pattern for RE$^+$ neurons and the relatively uniform, broadly tuned responses in GABAergic neurons. Accordingly, RE$^+$, but not CB$^+$ and GABAergic neurons, displayed a high 'population advantage' for odor classification (n = 19, 17 and 26 RE$^+$, CB$^+$ and GABAergic neuron populations; $t_{(34)} = 2.7$, $P = 0.03$ for RE$^+$ versus CB$^+$ comparison, other comparisons $P > 0.05$, unpaired t-tests with Holm-Bonferroni correction; **Fig. 7c**). Differences among neuronal subtypes were also apparent in the time course of decoding accuracy, with RE$^+$ and CB$^+$ populations showing earlier and sharper increases in decoding accuracy than GABAergic populations (**Fig. 7d**). Finally, we analyzed how random sampling

© 2016 Nature America, Inc. All rights reserved.

of different population sizes influenced odor classification accuracy for the three neuronal subtypes (**Fig. 7e**). For RE$^+$ neurons, and to a lesser extent CB$^+$ neurons, odor discrimination improved as the number of neurons in the population increased. Very large RE$^+$ populations (~100 neurons) discriminated the six odors with near-perfect accuracy (90% correct). By contrast, odor discrimination performance of GABAergic populations did not improve substantially with increasing population size.

DISCUSSION

Here we identified distinct cell types in LEC LII that exhibit specific connectivity to other brain areas and are differentially involved in odor encoding. The two excitatory cell types differ in their marker expression (RE versus CB), layer localization, morphology, intrinsic electrophysiological features and connectivity. Notably, RE$^+$, CB$^+$ and GABAergic neurons displayed distinct odor response properties. Hippocampus-projecting feedforward RE$^+$ neurons exhibited higher selectivity for different odors than feedback and contralaterally projecting CB$^+$ neurons. GABAergic neurons displayed the most broadly tuned odor-response profile. Odor discrimination performance was higher for RE$^+$ populations than CB$^+$ populations, and lowest for GABAergic populations.

Distinct spatial organization of RE$^+$ and CB$^+$ neurons in LII of the LEC

Our data demonstrate a segregation of RE$^+$ and CB$^+$ neurons within LII. RE$^+$ neurons form a band of densely packed neurons in LIIa, whereas CB$^+$ neurons cluster in LIIb. The clustering of CB$^+$ neurons in LEC is reminiscent of that reported for the MEC. In the MEC, however, the layering of the two cell populations is inverted. Thus, CB$^+$ islands are more superficial and are nested within a band of RE$^+$ neurons (ref. 23 and unpublished observations). The modular organization of RE$^+$ and CB$^+$ neurons in the LEC and MEC is intriguing, but its functional implications are enigmatic. It is noteworthy, though, that RE$^+$ and CB$^+$ neurons in MEC and LEC share two important features. First, RE$^+$ neurons in both LEC and MEC LII target the dentate gyrus, whereas CB$^+$ neurons project contralaterally and constitute a source for feedback projections (ref. 22 and this study). Second, encoding environmental features seems to be a common attribute of the two major principal cell types. In the MEC, both RE$^+$ and CB$^+$ neurons are spatially tuned[24,27]. Similarly, in the LEC both RE$^+$ and CB$^+$ neurons encode odors, albeit in different ways, as detailed below. In both areas, it is still unknown which functions set these two cell populations apart from each other.

Odor-selective RE$^+$ neurons project to the hippocampus

On the basis of previous studies and our own, it can be inferred that RE$^+$ neurons provide feedforward transmission of odor information from the sensory periphery to the core of the memory system, the hippocampus. Schwerdtfeger and colleagues demonstrated that fan cells in LII are directly innervated by mitral cell axons from the OB[17]. On the basis of morphological features and projection pattern, it is safe to assume that fan cells are identical with RE$^+$ neurons described in this study. As shown here, RE$^+$ neurons were the most selective and best tuned to their preferred odor among odor responsive neurons in LII. Their functional properties and direct connectivity with the dentate gyrus prompts inferences as to their putative function in olfactory memory. The ventral dentate gyrus is thought to support working memory for odor information[28]. Several studies have shown robust connectivity, especially between LEC and the ventral dentate gyrus[8]. Furthermore, there is evidence that the connection between LEC and the ventral dentate gyrus is crucially involved in successful odor pattern separation[29]. We hypothesize that the high percentage of odor-responsive RE$^+$ neurons and their high odor selectivity may subserve pattern separation in the dentate gyrus.

CB$^+$ neurons provide feedback information to olfactory areas

We identified several target areas of CB$^+$ neurons, namely OB, PIR and contralateral LEC. Interestingly, single CB$^+$ neurons can target both OB and PIR. This is in disagreement with findings reported by Chapuis and colleagues[2], who did not detect double-projecting LEC neurons. However, this discrepancy might simply result from differences in the techniques (use of rabies virus with low infectivity) and animal models (rats instead of mice). We agree with these authors that projecting neurons exhibit spatial segregation to some extent, as PIR-projecting neurons are located predominantly in the dorsal LEC, whereas neurons that project to the OB are located in the ventral LEC. Nevertheless, an intermediate stripe in the LEC contains neurons that establish connections with both target areas. These findings suggest a unique role for CB$^+$ neurons in LEC LIIb in the coordination of at least three regions in the brain: namely, OB, PIR and contralateral LEC. Accordingly, this neuronal population might have an important function in top-down modulation of olfactory processing.

We demonstrated that OB granule cells are excited by cortical feedback projections of CB$^+$ neurons. Activation of granule cells in the OB by cortical projections appears to be a general connectivity principle in the olfactory system[30,31]. Granule cells are highly interconnected and exert lateral inhibition onto mitral cells. Thus, feedback provided by CB$^+$ neurons could contribute to the decorrelation of mitral cell activity, thereby enhancing their selectivity, as suggested also for PIR input[32]. This in turn would lead to an improved discrimination of the input to the LEC. Notably, it has been suggested that the LEC establishes an anticipatory top-down modulation on the OB, as appreciable input from the LEC to the OB is present before the onset of the odor stimulation[33]. It is hence interesting to speculate that CB$^+$ neurons contribute to this modulatory effect.

Functional modulation of odor-evoked activity in the PIR mediated by feedback projections originating in the LEC has been shown consistently[2,34,35]. Experimental data from these studies suggest that the LEC exerts an inhibitory effect on the PIR, supporting the notion that excitatory LEC neurons control inhibitory neurons in the target area. We propose that CB$^+$ neurons are likely candidates for this modulatory effect on odor-evoked activity in the PIR.

GABAergic neurons exhibit broader odor tuning

GABAergic neurons in LEC LII are overall more broadly tuned to odor stimuli than their excitatory counterparts are. On the basis of these findings and the evident odor-responsiveness of most GABAergic neurons, we hypothesize a function in gain control rather than in merely increasing the signal-to-noise ratio of principal cells. The relatively nonselective response of GABAergic neurons can be brought about by convergent input from mitral cells from different glomeruli, as evident in the PIR[36], or by convergent input from surrounding excitatory neurons with different stimulus selectivity, similarly to findings reported for the MEC[37] and visual cortex[38].

Low selectivity of GABAergic neurons is reminiscent of what has been reported especially for PV$^+$ neurons in other brain regions[37–42]. Our immunohistochemistry data, however, revealed that PV$^+$ neurons are less prevalent in LEC LII than, for instance, in the neighboring MEC LII[43]. In fact, our results indicate that in LEC LII the majority of GABAergic neurons are 5-HT$_{3A}$R$^+$. Studies in other cortical areas attribute a non-fast firing pattern and broad stimulus tuning

© 2016 Nature America, Inc. All rights reserved.

to this cell type[44,45]. Interestingly, putative 5-$HT_{3A}R^+$ neurons (VIP^+ neurons) preferentially target other GABAergic neurons, thereby disinhibiting principal cells[46,47]. On the basis of these findings, we hypothesize that odor-responsive 5-$HT_{3A}R^+$ neurons in the LEC contribute to odor tuning of principal cells by releasing them from inhibitory control specifically during the presentation of odors.

Decoding performance argues for a population code of odor identity

The decoding performances of both RE^+ and CB^+ populations are better than those of GABAergic neurons and enable the extraction of odor identity from the population activity. RE^+ populations in particular display the highest information content, possibly because they comprise a mix of highly selective neurons responding to distinct odors. Thus, we suggest that upstream and downstream regions of the LEC in the olfactory system are supplied with odor information via a population code rather than by single cell activity, in analogy to what has been proposed for odor encoding in the PIR[13].

In summary, two distinct odor-responsive excitatory cell types are spatially segregated in LEC LII. Their long-range connectivity and differential odor representation indicate that they subserve different functions. RE^+ neurons transmit odor information to the hippocampus and might serve the formation of associative memories, whereas the input of CB^+ neurons to the OB might set the threshold for the responsiveness to odors, thus leading to adaptation of sensory responses.

METHODS

Methods and any associated references are available in the online version of the paper.

Note: Any Supplementary Information and Source Data files are available in the online version of the paper.

ACKNOWLEDGMENTS

We thank U. Amtmann for immunohistochemical work, E. Fuchs and A. Caputi for providing help at initial stages of the study and for proofreading the manuscript, and G. Giese and the staff from the MPI workshop for their technical assistance. All AAVs were obtained from Penn Vector Core, University of Pennsylvania, Philadelphia, USA. AAVs were provided by the GENIE Project and the Janelia Farm Research Campus of the HHMI and by K. Deisseroth, Stanford University. The research was funded by grants to H.M. from the European Research Council, FP 7 (ERC Adv. grant no. 250047), the German Research Foundation (DFG grants MO432/10 and SFB1134), and the German Ministry of Education and Research (BMBF) (grant 01GQ1003A).

AUTHOR CONTRIBUTIONS

F.C.L., S.M. and H.M. designed the experiments and wrote the manuscript with contributions from all authors. F.C.L. performed two-photon calcium imaging experiments, stereotactic injections and immunohistochemistry; S.M. and R.P. performed *in vivo* and *in vitro* electrophysiology and cell reconstructions; and H.L. and F.H. analyzed the calcium imaging data. P.H.S. was involved in discussing experiments and provided the infrastructure for the *in vivo* experiments.

COMPETING FINANCIAL INTERESTS

The authors declare no competing financial interests.

Reprints and permissions information is available online at http://www.nature.com/reprints/index.html.

1. Stäubli, U., Ivy, G. & Lynch, G. Hippocampal denervation causes rapid forgetting of olfactory information in rats. *Proc. Natl. Acad. Sci. USA* **81**, 5885–5887 (1984).
2. Chapuis, J. *et al.* Lateral entorhinal modulation of piriform cortical activity and fine odor discrimination. *J. Neurosci.* **33**, 13449–13459 (2013).
3. Igarashi, K.M., Lu, L., Colgin, L.L., Moser, M.-B. & Moser, E.I. Coordination of entorhinal-hippocampal ensemble activity during associative learning. *Nature* **510**, 143–147 (2014).
4. Boisselier, L., Ferry, B. & Gervais, R. Involvement of the lateral entorhinal cortex for the formation of cross-modal olfactory-tactile associations in the rat. *Hippocampus* **24**, 877–891 (2014).
5. Price, J.L. An autoradiographic study of complementary laminar patterns of termination of afferent fibers to the olfactory cortex. *J. Comp. Neurol.* **150**, 87–108 (1973).
6. Igarashi, K.M. *et al.* Parallel mitral and tufted cell pathways route distinct odor information to different targets in the olfactory cortex. *J. Neurosci.* **32**, 7970–7985 (2012).
7. Beckstead, R.M. Afferent connections of the entorhinal area in the rat as demonstrated by retrograde cell-labeling with horseradish peroxidase. *Brain Res.* **152**, 249–264 (1978).
8. Kerr, K.M., Agster, K.L., Furtak, S.C. & Burwell, R.D. Functional neuroanatomy of the parahippocampal region: the lateral and medial entorhinal areas. *Hippocampus* **17**, 697–708 (2007).
9. Steward, O. & Scoville, S.A. Cells of origin of entorhinal cortical afferents to the hippocampus and fascia dentata of the rat. *J. Comp. Neurol.* **169**, 347–370 (1976).
10. Shipley, M.T. & Adamek, G.D. The connections of the mouse olfactory bulb: a study using orthograde and retrograde transport of wheat germ agglutinin conjugated to horseradish peroxidase. *Brain Res. Bull.* **12**, 669–688 (1984).
11. Insausti, R., Herrero, M.T. & Witter, M.P. Entorhinal cortex of the rat: cytoarchitectonic subdivisions and the origin and distribution of cortical efferents. *Hippocampus* **7**, 146–183 (1997).
12. Eeckman, F.H. & Freeman, W.J. Correlations between unit firing and EEG in the rat olfactory system. *Brain Res.* **528**, 238–244 (1990).
13. Stettler, D.D. & Axel, R. Representations of odor in the piriform cortex. *Neuron* **63**, 854–864 (2009).
14. Sturgill, J.F. & Isaacson, J.S. Somatostatin cells regulate sensory response fidelity via subtractive inhibition in olfactory cortex. *Nat. Neurosci.* **18**, 531–535 (2015).
15. Young, B.J., Otto, T., Fox, G.D. & Eichenbaum, H. Memory representation within the parahippocampal region. *J. Neurosci.* **17**, 5183–5195 (1997).
16. Xu, W. & Wilson, D.A. Odor-evoked activity in the mouse lateral entorhinal cortex. *Neuroscience* **223**, 12–20 (2012).
17. Schwerdtfeger, W.K., Buhl, E.H. & Germroth, P. Disynaptic olfactory input to the hippocampus mediated by stellate cells in the entorhinal cortex. *J. Comp. Neurol.* **292**, 163–177 (1990).
18. Tahvildari, B. & Alonso, A. Morphological and electrophysiological properties of lateral entorhinal cortex layers II and III principal neurons. *J. Comp. Neurol.* **491**, 123–140 (2005).
19. Canto, C.B. & Witter, M.P. Cellular properties of principal neurons in the rat entorhinal cortex. I. The lateral entorhinal cortex. *Hippocampus* **22**, 1256–1276 (2012).
20. Canto, C.B., Wouterlood, F.G. & Witter, M.P. What does the anatomical organization of the entorhinal cortex tell us? *Neural Plast.* **2008**, 1–18 (2008).
21. Fujimaru, Y. & Kosaka, T. The distribution of two calcium binding proteins, calbindin D-28K and parvalbumin, in the entorhinal cortex of the adult mouse. *Neurosci. Res.* **24**, 329–343 (1996).
22. Varga, C., Lee, S.Y. & Soltesz, I. Target-selective GABAergic control of entorhinal cortex output. *Nat. Neurosci.* **13**, 822–824 (2010).
23. Ray, S. *et al.* Grid-layout and theta-modulation of layer 2 pyramidal neurons in medial entorhinal cortex. *Science* **343**, 891–896 (2014).
24. Tang, Q. *et al.* Pyramidal and stellate cell specificity of grid and border representations in layer 2 of medial entorhinal cortex. *Neuron* **84**, 1191–1197 (2014).
25. Fuchs, E.C. *et al.* Local and distant input controlling excitation in Layer II of the medial entorhinal cortex. *Neuron* **89**, 194–208 (2016).
26. Morales, M. & Bloom, F.E. The 5-HT3 receptor is present in different subpopulations of GABAergic neurons in the rat telencephalon. *J. Neurosci.* **17**, 3157–3167 (1997).
27. Domnisoru, C., Kinkhabwala, A.A. & Tank, D.W. Membrane potential dynamics of grid cells. *Nature* **495**, 199–204 (2013).
28. Kesner, R.P., Hunsaker, M.R. & Ziegler, W. The role of the dorsal and ventral hippocampus in olfactory working memory. *Neurobiol. Learn. Mem.* **96**, 361–366 (2011).
29. Weeden, C.S.S., Hu, N.J., Ho, L.U.N. & Kesner, R.P. The role of the ventral dentate gyrus in olfactory pattern separation. *Hippocampus* **24**, 553–559 (2014).
30. Markopoulos, F., Rokni, D., Gire, D.H. & Murthy, V.N. Functional properties of cortical feedback projections to the olfactory bulb. *Neuron* **76**, 1175–1188 (2012).
31. Boyd, A.M., Sturgill, J.F., Poo, C. & Isaacson, J.S. Cortical feedback control of olfactory bulb circuits. *Neuron* **76**, 1161–1174 (2012).
32. Otazu, G.H., Chae, H., Davis, M.B. & Albeanu, D.F. Cortical feedback decorrelates olfactory bulb output in awake mice. *Neuron* **86**, 1461–1477 (2015).
33. Kay, L.M. & Freeman, W.J. Bidirectional processing in the olfactory-limbic axis during olfactory behavior. *Behav. Neurosci.* **112**, 541–553 (1998).
34. Bernabeu, R., Thiriet, N., Zwiller, J. & Di Scala, G. Lesion of the lateral entorhinal cortex amplifies odor-induced expression of c-fos, junB, and zif 268 mRNA in rat brain. *Synapse* **59**, 135–143 (2006).
35. Mouly, A.M. & Di Scala, G. Entorhinal cortex stimulation modulates amygdala and piriform cortex responses to olfactory bulb inputs in the rat. *Neuroscience* **137**, 1131–1141 (2006).

© 2016 Nature America, Inc. All rights reserved.

36. Stokes, C.C.A. & Isaacson, J.S. From dendrite to soma: dynamic routing of inhibition by complementary interneuron microcircuits in olfactory cortex. *Neuron* **67**, 452–465 (2010).
37. Buetfering, C., Allen, K. & Monyer, H. Parvalbumin interneurons provide grid cell-driven recurrent inhibition in the medial entorhinal cortex. *Nat. Neurosci.* **17**, 710–718 (2014).
38. Hofer, S.B. *et al.* Differential connectivity and response dynamics of excitatory and inhibitory neurons in visual cortex. *Nat. Neurosci.* **14**, 1045–1052 (2011).
39. Kato, H.K., Gillet, S.N., Peters, A.J., Isaacson, J.S. & Komiyama, T. Parvalbumin-expressing interneurons linearly control olfactory bulb output. *Neuron* **80**, 1218–1231 (2013).
40. Miyamichi, K. *et al.* Dissecting local circuits: parvalbumin interneurons underlie broad feedback control of olfactory bulb output. *Neuron* **80**, 1232–1245 (2013).
41. Royer, S. *et al.* Control of timing, rate and bursts of hippocampal place cells by dendritic and somatic inhibition. *Nat. Neurosci.* **15**, 769–775 (2012).
42. Moore, A.K. & Wehr, M. Parvalbumin-expressing inhibitory interneurons in auditory cortex are well-tuned for frequency. *J. Neurosci.* **33**, 13713–13723 (2013).
43. Miettinen, M., Koivisto, E., Riekkinen, P. & Miettinen, R. Coexistence of parvalbumin and GABA in nonpyramidal neurons of the rat entorhinal cortex. *Brain Res.* **706**, 113–122 (1996).
44. Petersen, C.C.H. & Crochet, S. Synaptic computation and sensory processing in neocortical layer 2/3. *Neuron* **78**, 28–48 (2013).
45. Kerlin, A.M., Andermann, M.L., Berezovskii, V.K. & Reid, R.C. Broadly tuned response properties of diverse inhibitory neuron subtypes in mouse visual cortex. *Neuron* **67**, 858–871 (2010).
46. Pi, H.-J. *et al.* Cortical interneurons that specialize in disinhibitory control. *Nature* **503**, 521–524 (2013).
47. Lee, S., Kruglikov, I., Huang, Z.J., Fishell, G. & Rudy, B. A disinhibitory circuit mediates motor integration in the somatosensory cortex. *Nat. Neurosci.* **16**, 1662–1670 (2013).

© 2016 Nature America, Inc. All rights reserved.

ONLINE METHODS

Experimental animals. All mouse experiments were approved by the Regierungspräsidium Karlsruhe and followed the guidelines for animal treatment by German law (license Az G-74/13). Calcium imaging experiments and *in vivo* whole-cell patch clamp recordings were performed in 8- to 14-week-old male $GAD67^{Cre}$ mice[48], CB^{Cre} mice, $GAD67^{EGFP}$ mice[49] and wild-type mice with a C57BL/6 background. $GAD67^{EGFP}$ mice and 5-HT_3-EGFP[50] mice were used for immunohistochemistry. All animals were housed singly or in pairs and were kept on a 12 h light/dark cycle. Animals had no previous history of experimental treatment. All experiments were conducted during the light phase of the schedule, and investigators were not blind to the experimental condition, i.e. the mouse line.

Viral and tracer injections. We used AAV1.Syn.GCaMP6s (AV-1-PV2824, Penn Vector Core) in wild-type animals and AAV1.Syn.Flex.GCaMP6s (AV-1-PV2821, Penn Vector Core) in $GAD67^{Cre}$ and CB^{Cre} mice for the delivery of calcium indicators to the cells. The protocol for stereotactic injections was described previously[51]. Briefly, mice were anesthetized with a mixture of ketamine (120 mg/kg body weight) and xylazine (16 mg/kg, intraperitoneal injection), and mounted in a stereotactic apparatus (David Kopf Instruments, Tujunga, California) placed on a heat pad to keep the body temperature constant. Two small craniotomies were made above the LEC using a dental drill. The spots were located 3.8 mm posterior and 4.5 mm lateral of bregma, and 3.5 mm posterior and 4.8 mm lateral of bregma. A glass micropipette containing the virus was lowered 2.3 mm below the surface and then retracted to 1.6 mm while continuously injecting the virus (300 nl) over a period of 5 min.

We used CB^{Cre} mice to determine direct synaptic targets of CB^+ LEC neurons with axon terminals in the OB. AAV1.EF1.dflox.hChR2(H134R)-*mCherry* (AAV DIO *ChR2-mCherry*, AV-1-20297P) was obtained from Penn Vector Core. This AAV vector carries an inverted cassette coding for Channelrhodopsin-*2* fused to the fluorescent marker *mCherry*. In the presence of Cre recombinase, the cassette is inverted into the sense direction, and the fused proteins are expressed under the control of the EF1 promoter. The injections were targeted to both LEC (220 nl, −3.5 mm/4.8 mm/−2.2 mm) and *in vitro* electrophysiological slice recordings were performed 2–3 weeks post injection. Coordinates are given as anterior-posterior/medial-lateral/dorsal-ventral of bregma.

A similar protocol was used for the injection of retrograde tracers. The retrograde tracers CTB488, CTB555 (Life Technologies, Carlsbad, USA) or FG (0.5%, Fluorochrome, Denver, USA) were used for injection into the following brain areas: OB (CTB488 or CTB555, 300-450 nl, 4.7 mm/0.7 mm/−1.75 to −0.9 mm and 4.5 mm/1.0 mm/−1.75 to −0.9 mm), dentate gyrus (CTB555 or FG, 100 nl, −2.1 mm/1.75 mm/−2.0 mm), PIR (CTB555, 100 nl, 1.8 mm/2.9 mm/−3.5 mm) and LEC (CTB555, 100 nl; −3.5 mm/4.8 mm/−2.2 mm). The tracer was injected over a period of 5 min. The micropipette was left in place before retraction for additional 15 min to avoid spreading of the tracer in areas other than the target area.

Mice were excluded from further analysis if injections did not meet the following criteria: For calcium imaging experiments, mice with widespread and homogeneous labeling of LEC neurons were selected. For tracing studies, only mice with labeling restricted to the targeted areas were further analyzed.

Immunohistochemistry. Mice injected with retrograde tracers were subjected to histological analysis 5–7 days following CTB injection, or 2–3 weeks following FG injection. Animals that were used for electrophysiological recordings or two-photon imaging were subjected to immunohistochemical procedures directly after termination of the recording sessions. $GAD67^{EGFP}$ mice and 5-HT_3-EGFP mice were taken directly from their home cages. All mice were deeply anesthetized with isoflurane (Baxter, Germany) or ketamine/xylazine, and transcardially perfused with PBS, followed by 4% paraformaldehyde. Following removal from the skull, the fixed brains were kept in 4% paraformaldehyde at 4 °C for 12 h. The brains were sliced horizontally in 50-µm-thick sections. Free-floating sections were washed in PBS (pH 7.4) several times before they were permeabilized and blocked for 2 h in PBS (pH 7.4) containing 5% BSA and 0.2% Triton X-100. Sections were incubated over night at 4 °C in PBS containing 0.1% Triton X-100 with primary antibodies. For double-labeling experiments, slices were incubated simultaneously with the two primary antibodies. After thorough washing with PBS (pH 7.4), sections were incubated with the secondary antibody diluted in PBS (pH 7.4) for 2 h. Sections were washed repeatedly with PBS (pH 7.4), mounted on glass slides and covered with Aqua-Poly/Mount (Polysciences, Inc., Warrington, USA) or Mowiol 40-88 (Aldrich, Taufkirchen, Germany).

Antibodies. Primary antibodies: rabbit anti-CB (CB-38a, Swant), 1:5,000; mouse anti-CB (300, Swant), 1:2,000; mouse anti-CR (6B3, Swant), 1:1,000; mouse anti-NeuN (MAB377, Merck Millipore), 1:1,000; chicken anti-NeuN (ABN91, Merck Millipore), 1:1,000; mouse anti-PV (P3088, Sigma-Aldrich), 1:1,000; mouse anti-reelin (MAB5364, Merck Millipore), 1:2,000; rat anti-SOM (MAB354, Merck Millipore), 1:1,000; and rabbit anti-WFS1[52] (11558-1-AP, Proteintech), 1:1,000.

Secondary antibodies: Alexa Fluor 488 goat anti-mouse or anti-rabbit (A11029 and A11008, Life Technologies), 1:1,000; Cy3 goat anti-mouse (115-166-003, Jackson ImmunoResearch), 1:1,000; Cy3 donkey anti-rabbit (711-165-152, Jackson ImmunoResearch), 1:1,000; and Alexa Fluor 647 donkey anti-mouse or anti-rabbit (A31571 and A31573, Life Technologies), 1:1,000.

DAB staining. Brains from mice that were used for *in vivo* whole-cell patch-clamp experiments were further processed. After brain sections were stained with immunofluorescent markers as described above, they were further processed with diaminobenzidine (DAB) staining. Sections were quenched in 1% H_2O_2 for 10 min followed by thorough washing with PBS, before being permeabilized with 1% Triton X-100 in PBS for 1 h. After repeated washing, sections were incubated with avidin-biotin-horseradish peroxidase complex (Elite ABC, Vector Laboratories, Burlingame, USA) in PBS overnight at 4 °C. After washing with PBS, sections were incubated in a solution containing 0.04% DAB, 49.6% ammonium chloride buffer (0.08% ammonium chloride in PB), and 0.4% glucose oxidase to which 10% beta-D-glucose in H_2O (20 µl/ml) was added 1 min after start of the reaction. Sections were kept in the dark for 15–45 min. The reaction was stopped by washing sections again in PBS. Sections were mounted on glass slides using Mowiol 40-88.

Surgical procedure. Mice were anesthetized with a mixture of ketamine (120 mg/kg body weight) and xylazine (16 mg/kg, intraperitoneal injection). Additional doses were administered throughout the course of the surgery if necessary. Dexamethasone (0.02 ml at 3 mg/ml PBS) was intramuscularly injected into the quadriceps to reduce cortical stress response during the surgery and prevent cerebral edema. Lidocaine was administered locally to the skull as additional anesthetic for pain reduction. Animals were mounted in a stereotactic apparatus and placed on a heat pad to keep the body temperature constant. A small cut of approximately 1.5 cm was made in the skin and the underlying skull revealed. The skull was cleaned of periosteum, and muscles located laterally at the right side of the skull were removed. Four miniature screws (Bilaney Consultants, Kent, UK) were screwed into the skull and fixed with dental cement (Hager Werken, Duisburg, Germany). Orthogonal to each other, two cap nuts were cemented on top of the screws as anchors for holding bars, which allowed tilting the mouse by 90° to gain direct access to the LEC. A head plate was secured to the skull using dental cement and a small craniotomy was made. Regular rinsing with normal rat Ringer solution (NRR) (in mM: 135 NaCl, 5.4 KCl, 5 HEPES, 1.8 CaCl2, pH = 7.2 adjusted with NaOH) prevented the brain from overheating due to the drilling. The dura mater was removed leaving the underlying brain surface intact. Agarose (1.5% in NRR) was applied to the imaging window and a small round cover glass (thickness 100–150 µm, Warner Instruments, Hamden, USA) was placed on top. During the time of recording neuronal activity, urethane (Sigma-Aldrich, St. Louis, USA) was used for keeping the mouse anesthetized. However, in some instances when the mouse was still sufficiently anesthetized, the first few trials were recorded only under influence of the ketamine–xylazine mixture to avoid overdosing.

Two-photon calcium imaging *in vivo*. Two-photon imaging with olfactory stimulation was performed 6 to 8 d after virus injection. We used a ZEISS LSM 510 META NLO two-photon microscope (ZEISS, Jena, Germany) for calcium imaging experiments and *in vivo* whole-cell patch clamp recordings under visual guidance. The excitation source was a Chameleon Ultra mode-locked Ti:sapphire laser (Coherent, Santa Clara, USA) with the wavelength set to 900 nm. Two different water immersion objectives were used for the acquisition of fluorescence images. A 10×/0.3 NA Plan-Neofluar objective was used for overview images of the recording position, and an infrared-corrected 40×/1.0 NA objective for

© 2016 Nature America, Inc. All rights reserved.
npg

recordings of neuronal activity (both ZEISS, Jena, Germany). The mouse was tilted by 90° and fixed using a holding bar screwed to the cap nut on top of the skull. Fluorescence images of neuronal activity were acquired at 5 Hz frame rate (100 × 100 pixels; longpass 515 nm filter). A high-resolution image was acquired as reference image (512 × 512 pixels, line average 4). The laser excitation wavelength was set to 750 nm for the acquisition of images from neurons labeled with the retrograde tracer CTB555. Spectral separation between signal emitted by GCaMP6 and CTB555 was achieved by using bandpass emission filters (500–550 nm and 575–640 nm). We recorded 2–4 different areas in the LEC per mouse. In some mice, Vybrant DiI cell-labeling solution (Life Technologies, Carlsbad, USA) was injected through the imaging window after the recording session to confirm *ex vivo* the correct location of the window. The experiment was terminated by deeply anesthetizing the mouse with isoflurane before perfusing it as described above. The brain was used for analysis of injection sites, location of the imaging window and retrograde tracer labeling and for immunohistochemical experiments. If calcium image quality did not meet our criteria—i.e., when surgical procedures resulted in bleeding at the brain surface or when image motion artifacts were too strong—mice were excluded from further analysis.

Olfactory stimulation. Olfactory stimulation was controlled with custom-written software in LabView. Monomolecular odors with a broad spectrum of molecular features were chosen for stimulating neuronal activity in the LEC: ethyl butyrate (EB), amyl acetate (AA), eugenol (E), cineole (C), hexanal (H) and benzaldehyde (B) (Sigma-Aldrich, ST. Louis, USA). A custom-built flow-dilution olfactometer mixed saturated odor vapor of pure odors with filtered air. The carrier stream of clean air was set to a flow rate of 2 l per minute, which was mixed with odorized air of 0.2 l per minute for a final concentration of 10%. In an additional set of experiments, two of the odors (benzaldehyde and amyl acetate) were diluted with mineral oil and presented at different concentrations (**Supplementary Fig. 3**). Odors were delivered by a tubing system and solenoid valves under computer control for 4 s per stimulus with an initial delay of 5 s for baseline recordings. The tube opening was positioned <1 cm in front of the animal's nostrils. The delay in odor onset resulting from the stimulation apparatus (tubing etc.) was determined to be 330 ms as measured using a photoionization detector, and was taken into account in the analysis. The mouse was allowed to breathe freely and stimulus delivery was not locked to the respiration cycle. Each stimulus was followed by an interstimulus interval (ISI) of 26 s to avoid sensory adaptation. At least 15 trials were recorded for every imaging area with each trial consisting of 3 stimuli presented in a randomized fashion. Every series of trials included mock trials of pure filtered clean air. We used a suction system positioned next to the tube opening to quickly remove lingering odor. The flow rate of odorized air was continuously controlled by a mass flow sensor for gases (First Sensor AG, Berlin, Germany).

Acquisition of brain slice images. The analysis of brain sections focused on dorsal and intermediate parts of the LEC, as these anatomical levels correlated to the accessible part of the LEC using the surgical procedure for two-photon microscopy. Images of all brain slices with fluorescence staining, tracer injections or virus injections were taken with a confocal laser scanning microscope (LSM 700, software ZEN 2010, ZEISS, Germany) equipped with a 20× objective. Images for quantification of retrogradely labeled neurons and expression of marker proteins were taken with 1,024 × 1,024 pixel resolution and 640 µm × 640 µm image size. *GAD67*^{EGFP} mice were used for the analysis of the relative percentages of excitatory RE$^+$, excitatory CB$^+$ and GABAergic neurons in LIIa and LIIb. We employed immunohistochemical staining against RE and WFS1. The latter was used to quantify excitatory CB$^+$ neurons (**Supplementary Fig. 1**). *GAD67*^{EGFP} mice and 5-HT$_3$-EGFP mice were used for the analysis of protein marker expression of GABAergic neurons. We used immunohistochemical staining against RE and against CB in 5-HT$_3$-EGFP mice to distinguish between LIIa and LIIb, and counted in these mice only 5-HT$_3^+$/EGFP$^+$ neurons. To estimate the percentage of 5-HT$_{3A}$R$^+$ neurons in the total GABAergic population, we compared the number of EGFP$^+$ cells in 5-HT$_3$-EGFP mice with the number of EGFP$^+$ cells in the *GAD67*^{EGFP} mice. We analyzed 4 to 8 sections from each hemisphere. The software ImageJ (NIH) was used for further processing of images. Data are presented as mean ± s.e.m., if not indicated otherwise.

***Analysis of in vivo* two-photon calcium imaging data.** Image analysis was performed in Matlab (MathWorks, Natick, MA) and ImageJ (NIH). All quantifications and statistical analyses were performed with Matlab. Somatic regions of interest (ROIs) were manually selected on high-resolution reference images. Calcium imaging movies were warped to high-resolution reference images by custom-written routines based on nonlinear image registration. For each ROI, the average fluorescence intensity was extracted and converted into relative change in calcium according to

$$\frac{\Delta F}{F} = \frac{F - F_0}{F_0}$$

Baseline fluorescence F_0 was calculated as the tenth percentile of background-subtracted fluorescence for each ROI. Mean $\Delta F/F$ level during the 4-s pre-stimulus period was subtracted from each individual odor response. Odor-evoked receptive fields were computed by averaging calcium responses to all presentations of a specific odor and sorted from 'best' to 'worst' based on the mean $\Delta F/F$ value during a time window 2 to 3 s after stimulus onset (where typically the early response peak occurred; **Supplementary Fig. 10**). Trial-averaged fluorescence traces were defined as significant 'early' responses, when $\Delta F/F$ either increased ('positive' responses) or decreased ('negative' responses) by more than three times the baseline s.d. during the 4-s stimulation time window. The duration of significant positive calcium responses was calculated as their full-width at half-maximum (FWHM), fully opening the analysis window to 0–20 s following stimulus onset. Onset latencies of calcium transients were determined for 'early' responses (within the 4-s stimulation period) by linearly fitting the time points between stimulus onset and threshold crossing (plus two extra frames) and extrapolating the resulting fit line back to zero baseline crossing. Onset latencies were corrected for the 0.33-s dead time determined for odor delivery. 'Late' responses occurring after stimulation offset were defined as additional positive $\Delta F/F$ peaks during a 4-s window after stimulus end exceeding the mean $\Delta F/F$ value during the last second of the stimulus period by more than three s.d. calculated within this window.

We quantified odor tuning (selectivity of responses to specific odors) by normalizing the ranked odor-evoked amplitudes to the mean amplitude of the best-odor responses. The sharper the decline in amplitude for second-best and further odors, the higher the selectivity. Additionally, we assessed selectivity by calculating the kurtosis of the $\Delta F/F$ responses for each odor as a measure of 'lifetime sparseness' (**Supplementary Fig. 11**). Finally, as another measure of selectivity, we determined the fraction of neurons responding to zero, one, or multiple odors (positively or negatively) for each cell type. Mutual information between odor stimulation and binned calcium responses was computed as described in Abbott and Dayan, *Computational Neuroscience*[53], Chapter 4 (and see **Supplementary Fig. 12**).

Odor classification analysis was performed with a probabilistic Bayesian classifier, as implemented in the Matlab Statistics toolbox (NaiveBayes class). Neuronal responses (predictors) were modeled with a normal distribution. For each odor, the classifier estimated a separate distribution based on mean and s.d. in the training data set for this odor. During prediction, the posterior probability of a test response originating from each odor stimulation was computed, and the test data were classified according to the largest posterior probability (i.e. the most likely odor). Cross-validation was performed by leaving out 10% of the trials per iteration, and testing classifier performances on the omitted data. Average classifier performance was determined as mean over 100 iterations.

Electrophysiological recordings. Whole-cell patch-clamp recordings in the LEC were performed *in vitro* and *in vivo*. For *in vivo* recordings, mice were anesthetized with ketamine–xylazine and a craniotomy above the LEC was made as described above for two-photon calcium imaging experiments. Cells were patched in the LEC under visual guidance using the two-photon microscope, which allowed for specific selection of various cell types based on their EGFP or GCaMP6 expression. CTB/GCaMP6 double positive cells were selected for whole-cell patch-clamp recordings of odor responsive principal cells in LIIa. To test for odor responsiveness, two-photon calcium imaging was performed before patching as described above using shorter interstimulus intervals (10 s) and fewer trials (each odor was presented at least twice). In some cases, movement of the brain was reduced by applying a thin layer of low melting point agarose (Thermo Fisher Scientific, Waltham, USA) with a concentration of 1.5% in NRR.

© 2016 Nature America, Inc. All rights reserved.
npg

doi:10.1038/nn.4303

Recording pipettes were pulled from borosilicate glass capillaries with resistances of 4.5–6.0 MΩ and were filled with intracellular solution containing (in mM) 130 potassium gluconate, 10 sodium gluconate, 10 HEPES, 10 phosphocreatine-Na, 4 NaCl, 4 Mg-ATP, 0.3 GTP, pH 7.2 adjusted with KOH. Texas Red (4 µl/ml) was added to the intracellular solution to visualize the pipette under the microscope. No correction was applied for liquid junction potentials. Before penetration of the pia, high pressure (300 mbar) was applied to the pipette. Directly after penetration of the pia, the pressure was quickly reduced to 50 mbar. The pressure was further lowered to 30 mbar as soon as the pipette was close to the cell. For the analysis of firing patterns, 1 s current pulses were applied in current-clamp mode, starting with a −50 pA pulse, followed by pulses that increased incrementally in 20 pA steps, until saturation was reached. Interpulse interval was set to 3 s. Saturation was recognized as a decrease in action potential amplitudes. Series resistance was monitored in voltage-clamp mode measuring peak currents in response to small hyperpolarizing pulses. Series resistances of up to 50 MΩ were accepted. Signals were sampled at 10 kHz and filtered at 3 kHz. PulseSoftware (HEKA) was used for stimulus delivery and data acquisition. Matlab was used for offline analysis of firing patterns. Sag was calculated from the first hyperpolarizing sweep as the difference between maximal and steady state deflection in percent of the steady state deflection. Initial, middle and final interspike interval was calculated from the sweep with the maximal firing frequency. Adaptation was calculated as initial interspike interval/final interspike interval multiplied by 100 subtracted from 100. Firing pattern traces represent the first hyperpolarizing sweep, the sweep with the first action potentials and the sweep with maximal firing frequency. Note that in some cases action potentials occurred spontaneously during the first sweep. In other cases, maximal firing frequency was reached during the sweep with the first action potential. In both cases, only two traces are shown.

For *in vitro* patch-clamp recordings, mice were deeply anesthetized with inhaled isoflurane, and transcardially perfused with ~30 ml ice-cold sucrose solution oxygenated with carbogen gas (95% O_2, 5% CO_2, pH 7.4). Mice were decapitated and brains removed. Horizontal 300 µm thick sections were cut on a slicer in ice-cold oxygenated sucrose solution containing (in mM) 252 sucrose, 3 KCl, 1.25 $Na_2H_2PO_4$, 24 $NaHCO_3$, 2 $MgSO_4$, 2 $CaCl_2$ and 10 glucose. Slices were incubated in oxygenated Ringer's extracellular solution containing 125 mM NaCl, 25 mM $NaHCO_3$, 1.25 mM NaH_2PO_4, 2.5 mM KCl, 2 mM $CaCl_2$, 1 mM $MgCl_2$ and 25 mM glucose at 32 °C for ~15 min, and subsequently at RT until used for recordings. Whole-cell patch-clamp recordings were performed at 30–32 °C using pipettes pulled from borosilicate glass capillaries with resistances of 3–5 MΩ (for LEC neurons) and 6–8 MΩ (for OB cells). Intracellular solution for *in vitro* recordings was the same as for *in vivo* recordings. Sections were continuously perfused with oxygenated extracellular solution. Cells were visualized by an upright microscope equipped with infrared-differential interference contrast and standard epifluorescence. Settings for data acquisition, analysis and presentation were the same as for *in vivo* recordings except that injected currents started with −200 pA pulses and series resistance did not increase above 25 MΩ. PatchMaster (HEKA) was used for stimulus delivery and data acquisition. Matlab and IgorPro were used for offline analysis of firing patterns.

To investigate synaptic inputs, cells were analyzed at a holding potential of −70 mV and axonal fibers were stimulated with blue laser light. PSCs were recorded in response to 5 ms laser stimulations (473 nm) using approximately 120 mW/mm^2 laser power. Glutamatergic and GABAergic synaptic inputs were tested by adding the following pharmacological agents via bath-application: gabazine (10 µM; SR 95531 hydrobromide), D-AP5 (50 µM) and CNQX (10 µM). FitMaster (HEKA) was used for offline analysis of PSCs.

***K*-means cluster analysis.** *K*-means clustering was performed in Matlab using the distance measure 'sqeuclidean' and 1,000 replicates, based on electrophysiological parameters as shown in **Supplementary Figure 6a**. Note that AHP and AP amplitude had to be excluded from this analysis to obtain good cluster results (>90% accuracy), suggesting that these two parameters are not characteristic for CB^+ and RE^+ cells. All parameters were standardized using the z-score function in Matlab.

Biocytin filling and cell reconstruction. For morphological analysis of electrophysiologically identified target cells, whole-cell patch-clamped neurons were filled with biocytin (Aldrich, Taufkirchen, Germany; 10 mg/ml, dissolved in intracellular solution). Cells were filled for up to 8 min before retracting the pipette. Only one neuron per mouse or brain slice was patched and filled to enable unambiguous reconstruction. Following *in vivo* filling, mice were deeply anesthetized with isoflurane, and transcardially perfused with PBS and paraformaldehyde as described above. The dissected brain or the acute slices with filled cells were fixed overnight in 4% paraformaldehyde. Whole brains were sliced on a vibratome (VT1000s vibratome, Leica, Germany) into 50 µm thick horizontal slices, and stained with antibodies against several protein markers before staining with DAB as described above. Labeled neurons were reconstructed from up to 55 serial slices per cell using Neurolucida software (MicroBrightField, Colchester, Vermont).

Statistics. Data collection and analysis were not performed blind to the conditions of the experiments. We did not use statistical methods to predetermine sample size, but our sample sizes are similar to those generally employed in the field. For calcium imaging data, means between different cell types were compared by parametric statistical tests. Data are shown as mean ± s.e.m. and all *P*-values were adjusted for multiple comparisons using the Bonferroni procedure. For electrophysiological data, the Shapiro-Wilk test was used to test for normal distribution. Normally distributed data were then tested for equal variability using the *F*-test. Non-parametric data were tested with the Filgren-Killeen test. Normally distributed data are shown as mean ± s.e.m., and were compared using the unpaired *t*-test either for equal or unequal variability. Non-normally distributed data with equal variability are shown as median ± interquartile range, and were compared using the Mann-Whitney *U* test. All *P*-values were corrected with the Holm-Bonferroni test to control for familywise error rates. Non-normally distributed data with unequal variability were not statistically compared. Graphs were made with Excel (Microsoft) and Matlab. The figures were assembled in Illustrator (Adobe). The following code was used for *P*-values in our figures: $*P < 0.05$; $**P < 0.01$; $***P < 0.001$.

A **Supplementary Methods Checklist** is available.

Data availability. The data that support the findings of this study are available from the corresponding author upon request.

Code availability. Custom-written Matlab scripts can be made available to any interested scientist.

48. Tolu, S. *et al.* A versatile system for the neuronal subtype specific expression of lentiviral vectors. *FASEB J.* **24**, 723–730 (2010).
49. Tamamaki, N. *et al.* Green fluorescent protein expression and colocalization with calretinin, parvalbumin, and somatostatin in the GAD67-GFP knock-in mouse. *J. Comp. Neurol.* **467**, 60–79 (2003).
50. Inta, D. *et al.* Neurogenesis and widespread forebrain migration of distinct GABAergic neurons from the postnatal subventricular zone. *Proc. Natl. Acad. Sci. USA* **105**, 20994–20999 (2008).
51. Cetin, A., Komai, S., Eliava, M., Seeburg, P.H. & Osten, P. Stereotaxic gene delivery in the rodent brain. *Nat. Protoc.* **1**, 3166–3173 (2006).
52. Kitamura, T. *et al.* Island cells control temporal association memory. *Science* **343**, 896–901 (2014).
53. Abbott, L.F. & Dayan, P. *Theoretical Neuroscience: Computational and Mathematical Modeling of Neural Systems* (MIT Press, 2001).

© 2016 Nature America, Inc. All rights reserved.